

Uncovering the behavior of $\text{Hf}_2\text{Te}_2\text{P}$ and the candidate Dirac metal $\text{Zr}_2\text{Te}_2\text{P}$

K. -W. Chen,^{1,2} S. Das,^{1,2} D. Rhodes,^{1,2} S. Memaran,^{1,2} T. Besara,¹

T. Siegrist,^{1,3} E. Manousakis,^{1,2} L. Balicas,¹ and R. E. Baumbach¹

¹*National High Magnetic Field Laboratory, Florida State University*

²*Department of Physics, Florida State University and*

³*Department of Chemical and Biomedical Engineering, Florida State University*

(Dated: February 12, 2016)

Results are reported for single crystal specimens of $\text{Hf}_2\text{Te}_2\text{P}$ and compared to its structural analogue $\text{Zr}_2\text{Te}_2\text{P}$, which was recently proposed to be a potential reservoir for Dirac physics.[1] Both materials are produced using the iodine vapor phase transport method and the resulting crystals are exfoliable. The bulk electrical transport and thermodynamic properties indicate Fermi liquid behavior at low temperature for both compounds. Quantum oscillations are observed in magnetization measurements for fields applied parallel but not perpendicular to the c -axis, suggesting that the Fermi surfaces are quasi-two dimensional. Frequencies are determined from quantum oscillations for several parts of the Fermi surfaces. Lifshitz-Kosevich fits to the temperature dependent amplitudes of the oscillations reveal small effective masses, with a particularly small value $m^* = 0.046m_0$ for the α branch of $\text{Zr}_2\text{Te}_2\text{P}$. Electronic structure calculations are in good agreement with quantum oscillation results and illustrate the effect of a stronger spin-orbit interaction going from Zr to Hf. These results suggest that by using appropriate tuning parameters this class of materials may deepen the pool of novel Dirac phenomena.

I. INTRODUCTION

Efforts in condensed matter physics during the past century have focused on states of matter that are characterized by their symmetry. This encompasses phenomena such as magnetism, superconductivity, charge density wave order, nematicity, etc. and was foundational for development of society transforming modern technologies: e.g., those based on rare earth magnets and superconductors. Another type of ordering has recently gained prominence, where the electronic state is characterized by its topology instead of a broken symmetry. The first examples of this were the quantum Hall effect and fractional quantum Hall effect (e.g., in GaAs/AlGaAs)^{2,3} and during the past decade this field has rapidly expanded to include new families of topological materials, particularly those with three dimensional crystalline structures. These three dimensional Dirac materials host topologically protected linearly dispersing (“photon-like”) electronic bands both in the bulk and as surface states.⁴ There are various origins for this behavior including strong spin-orbit coupling (e.g., topological insulators Bi_2Te_3 ^{5–7} and Bi_2Se_3 ^{5,7,8}), crystalline symmetries (e.g., Dirac semimetals Cd_3As_2 ^{9,10} and Na_3Bi ^{11,12}), combinations of these effects (Weyl semimetals (Nb,Ta)(P,As)^{13–16}), and strong electronic correlations (Kondo insulators SmB_6 ^{17–19}).

Given their novel physics and potential practical applications,^{4,16,20} there is great interest in diversifying the pool of 3D Dirac materials. Taking inspiration from earlier successes in condensed matter physics, this will be accomplished largely through tuning of known systems (and new materials as they are uncovered) using control parameters such as magnetic fields, applied pressure, chemical substitution, nanostructuring, and device fabrication. This route not only gives insight into par-

ent compounds, but also has a high likelihood of uncovering transformative phenomena. This approach has already proven successful for some topological systems: in Cd_3As_2 both applied pressure²¹ and point contact experiments²² stabilize superconductivity and may provide a route towards studies of Majorana fermions.

$\text{Zr}_2\text{Te}_2\text{P}$ was recently introduced as a possible strongly topological metal with multiple Dirac cones: i.e., a Dirac metal when exfoliated into a few atomic layers.¹ Of particular interest is that this compound crystallizes in the well-known tetradamite structure and is easily exfoliated, opening the way for device development. In order to explore the effect of a strengthened spin-orbit interaction in this system, we undertook to synthesize related compounds with larger Z elements. Here we report the synthesis and bulk characterization of the isoelectronic analogue $\text{Hf}_2\text{Te}_2\text{P}$, which forms in the same structure, is easily exfoliated, and supports similar bulk electrical transport and thermodynamic behavior. Quantum oscillations are observed in both compounds starting near magnetic fields of $H = 3$ T, opening the possibility of experimentally comparing their Fermi surfaces and characterizing the Dirac behavior through the Berry’s phase. We additionally present electronic structure calculations which reveal the effect of a strengthening spin-orbit interaction going from Zr to Hf.

II. METHODS

Single crystals of $\text{Zr}_2\text{Te}_2\text{P}$ and $\text{Hf}_2\text{Te}_2\text{P}$ were grown from elements as previously described for the Zr version.²³ Stoichiometric polycrystalline precursor material was first prepared by reacting the raw elements at 1000 °C for 24 hours. The resulting powders (1.5 g and 1.3 g for $\text{Zr}_2\text{Te}_2\text{P}$ and $\text{Hf}_2\text{Te}_2\text{P}$, respectively) were

subsequently sealed under vacuum with 46 mg of iodine in quartz tubes with 18 mm diameter, 2 mm thickness, and 10 cm length. The tubes were placed in a resistive tube furnace with a temperature gradient with hot and cold zone temperatures of 900 and 800 °C, respectively. The ampoules were held under these conditions for three weeks and then quenched to room temperature. Large hexagonal single crystals formed near the cold zone. For $\text{Zr}_2\text{Te}_2\text{P}$ the linear dimensions are as large as $10 \times 10 \times 0.4$ mm. $\text{Hf}_2\text{Te}_2\text{P}$ crystals were slightly smaller, with dimensions $3 \times 3 \times 1$ mm (Fig. 1).

X-ray diffraction measurements were collected using a Scintag PAD-V $\Theta:2\Theta$ diffractometer using Cu K-alpha radiation. The sample consisted of crushed crystals spread randomly on a glass slide. Due to the tendency of the crystals to separate as plates in the ab -plane, completely random orientation was not achieved, and the XRD pattern shows signs (001) texture. The pattern was fit with the WINPREP software²⁴ using the known parameters of the isostructural compound $\text{Zr}_2\text{Te}_2\text{P}$ as starting parameters.

Flakes of $\text{Zr}_2\text{Te}_2\text{P}$ and $\text{Hf}_2\text{Te}_2\text{P}$ were exfoliated from bulk crystals using the micromechanical cleavage technique with adhesive scotch-tape and transferred onto a p -doped silicon wafer substrate covered with a 270 nm layer of SiO_2 . Atomically-thin crystals were identified under an optical microscope using optical contrast. Atomic Force Microscopy (AFM) imaging was performed using an Asylum Research MFP-3D AFM system. Images were taken about 2 hours after exfoliation, during which the samples were exposed to air.

Zero magnetic field electrical resistivity ρ was measured using the ³He option in Quantum Design Physical Properties Measurement System for temperatures 400 mK $< T < 300$ K. Several individual crystals were measured for each concentration, which revealed a high degree of batch uniformity. Heat capacity C measurements were performed using the same apparatus for temperatures 400 mK $< T < 20$ K. Magnetization $M(T, H)$ measurements were undertaken for single crystals for temperatures $T = 1.8 - 300$ K under an applied magnetic field of $H = 10$ kOe applied parallel \parallel and perpendicular \perp to the c -axis using a Quantum Design Magnetic Property Measurement System. Magnetic susceptibility χ is defined as the ratio M/H .

Electronic structure calculations were performed using the Vienna *ab-initio* simulation package^{25–28} (VASP) within the generalized gradient approximation (GGA). The contribution from the spin-orbit coupling is included in the calculations. The Perdew-Burke-Ernzerhof (PBE) exchange correlation functional²⁹ and the projected augmented wave (PAW) methodology³⁰ were used to describe the core electrons. The 4s, 4p, 5s, and 4d electrons for Zr, the 5s, 5p, 6s, and 5d electrons for Hf, the 4d, 5s and 5p electrons for Te, and the 3s and 3p electrons for P were treated as valence electrons in all calculations. The energy cut off for the plane-wave basis was chosen to be 400 meV. A total of 240 bands and a k -point mesh of

$20 \times 20 \times 4$ were used for the self-consistent ground state calculations. A total of 100 k -points were chosen between each pair of special k -points in the Brillouin-zone for the band-structure calculations. The Fermi surfaces were generated with a k -point mesh of $20 \times 20 \times 4$, using the eigenvalues obtained from VASP and were visualized using the XCrysden software.³¹

III. RESULTS AND DISCUSSION

Results from powder X-ray diffraction measurement of crushed $\text{Hf}_2\text{Te}_2\text{P}$ crystals are shown in Fig. 1, along with a pattern fit. Parameters of the isostructural compound $\text{Zr}_2\text{Te}_2\text{P}$, which crystallizes in the space group $R\bar{3}m$ (#166), were used as starting parameters. The fit yielded lattice parameters $a = 3.7946(2)$ Å and $c = 29.140(1)$ Å, and displayed no traces of impurity phases. The lattice parameters are smaller than the $\text{Zr}_2\text{Te}_2\text{P}$ parameters ($a = 3.8119(3)$ Å and $c = 29.189(3)$ Å),²³ indicative of the smaller ionic radius of Hf compared to Zr.³²

Atomic force microscopy (AFM) results for exfoliated flakes of $\text{Zr}_2\text{Te}_2\text{P}$ and $\text{Hf}_2\text{Te}_2\text{P}$ are shown in Figs. 1d,e. Edge step profiles reveal that the crystals are easily reduced to single- or several-unit cell flakes, where the edge step can be the same size as a single c -axis unit cell. Samples that are left exposed to air are seen to change over time, revealing that these specimens are air sensitive.

Electrical resistance normalized to its room temperature value $R/R_{300\text{K}}$ as a function of temperature T data are shown in Fig. 2a for $\text{Zr}_2\text{Te}_2\text{P}$ and $\text{Hf}_2\text{Te}_2\text{P}$, where the electrical current was applied in the basal ab -plane. Metallic behavior is observed for both materials, with room temperature resistivities $\rho_{300\text{K}} \approx 60 - 80$ $\mu\Omega\text{cm}$, depending on uncertainty of the geometric factor. $R/R_{300\text{K}}$ decreases linearly with decreasing temperature down to $T \approx 50$ K, where the resistance begins to saturate in a Fermi-liquid like manner. For both compounds, the resistivity saturates near $3 - 5$ $\mu\Omega\text{cm}$, giving a residual resistivity ratio $RRR = R_{300\text{K}}/R_0 \approx 20$. This value for RRR is not particularly large, and might be taken to indicate appreciable disorder scattering. Alternatively, it is possible that as-cast crystals have large RRR but rapidly begin to degrade after being exposed to atmosphere. As shown below, quantum oscillations are easily observed in magnetization measurements, which is unexpected if there is large disorder scattering.

The temperature dependences of the heat capacity C divided by T are shown in Figs. 2b,c for $\text{Zr}_2\text{Te}_2\text{P}$ and $\text{Hf}_2\text{Te}_2\text{P}$. Fermi liquid behavior is seen for both compounds, where the expression $C/T = \gamma + \beta T^2$ describes the data for 500 mK $< T < 10$ K. Fits to the data give $\gamma = 5.4$ mJ/mol-K² and 4.7 mJ/mol-K² and $\beta = 0.62$ and 0.71 mJ/mol-K⁴ for $\text{Zr}_2\text{Te}_2\text{P}$ and $\text{Hf}_2\text{Te}_2\text{P}$, respectively. That the electronic coefficients of the heat capacity γ are similar for both compounds is consistent with electronic structure calculations presented below, where the total

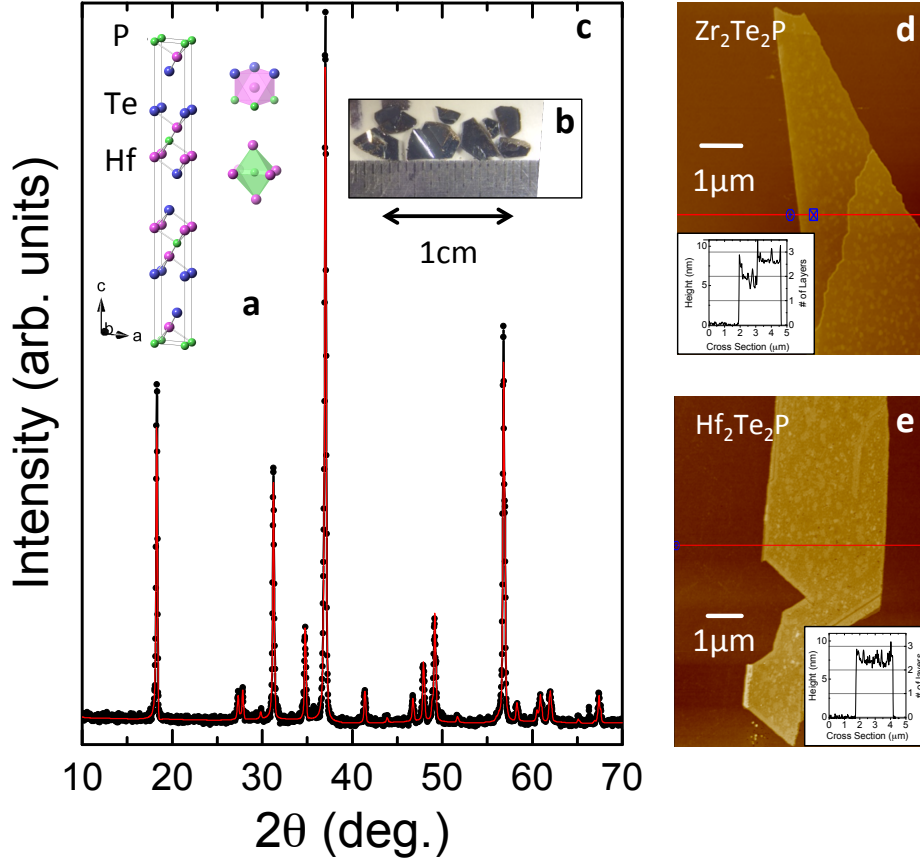


FIG. 1. (a) Unit cell of the $M_2\text{Te}_2\text{P}$ ($M = \text{Zr}$ and Hf) compounds. (b) Single crystal specimens of $\text{Hf}_2\text{Te}_2\text{P}$. (c) Powder x-ray diffraction pattern for $\text{Hf}_2\text{Te}_2\text{P}$. The solid red line is a pattern fit to the data to determine lattice parameters. (d) Atomic Force Microscopy (AFM) image collected from an atomically thin flake of $\text{Zr}_2\text{Te}_2\text{P}$ on a SiO_2 substrate. Inset: Height Profile (along the red line shown in the image) indicating a thickness of approximately 6 nm equivalent to two unit cells. (e) AFM image for $\text{Hf}_2\text{Te}_2\text{P}$. Inset: Height profile for two-unit cell flake.

density of states at the Fermi energy remains roughly constant upon going from Zr to Hf. From the expression $\beta = r1944(T/\theta_D)\text{J/mol-K}$, where r is the number of atoms per formula unit, the Debye temperatures θ_D are calculated to be 250 K and 239 K for the Zr and Hf compounds, respectively. This result is consistent with the increased atomic mass of Hf in comparison to Zr.

Fig. 3 displays magnetization M as a function of the field H applied either parallel \parallel or perpendicular \perp to the c -axis and for both compounds. $M(H)$ is diamagnetic for $H \perp c$, whereas curves for $H \parallel c$ initially are paramagnetic with increasing H , but eventually take on negative slopes, and even become negative for $\text{Hf}_2\text{Te}_2\text{P}$. The initial positive slopes can be attributed to a small fraction of paramagnetic impurities. In the insets, the magnetic susceptibilities $\chi = M/H$ for $\text{Zr}_2\text{Te}_2\text{P}$ and $\text{Hf}_2\text{Te}_2\text{P}$ are shown, where diamagnetic behavior with little anisotropy is observed at large temperatures. Weak upturns are seen at low T , which may be due to Curie tails from paramagnetic impurities. Quantum oscillations are observed starting from low fields for both compounds when $H \parallel$

c . The very low field for onset of oscillations indicates the high sample quality. QOs are not seen when $H \perp c$, giving strong evidence that the Fermi surface is two dimensional. While this is expected from the band structure calculations presented below, further angle resolved measurements will be useful to illustrate the degree of two dimensionality.

The quantum oscillations in the magnetization ΔM are isolated by subtracting a 3rd order polynomial background as shown in Fig. 4 for different temperatures T between 1.8 K and 30 K over the field range $H = 3 \text{ T} - 7 \text{ T}$. Fast Fourier transforms (FFT) for ΔM at various temperatures were performed using a Hanning window to extract the oscillation frequencies (Figs. 4b,e). The FFTs yield frequencies $F_\alpha = 11.4 \text{ T}$ and $F_\beta = 89.9 \text{ T}$ for $\text{Zr}_2\text{Te}_2\text{P}$ and $F_\gamma = 106.8 \text{ T}$ and $F_\eta = 146.6 \text{ T}$ for $\text{Hf}_2\text{Te}_2\text{P}$, as summarized in Table I. The temperature dependences of the FFT amplitude are shown in Figs. 4c,f. The solid lines are fits to the data according to the thermal damping factor R_T of the Lifshitz-Kosevich formula using the expression,

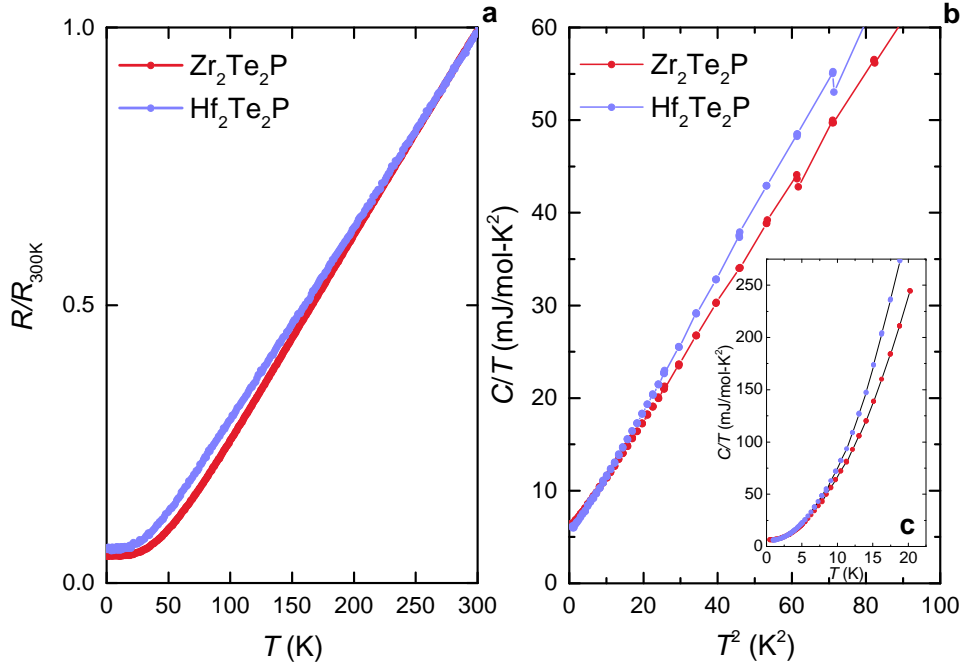


FIG. 2. (a) Room temperature normalized electrical resistance R/R_{300K} for M_2Te_2P ($M = Zr$ and Hf). (b) Heat capacity C divided by temperature T vs. T^2 for M_2Te_2P ($M = Zr$ and Hf) showing linear behavior as expected for a Fermi liquid. (c) C/T vs T for M_2Te_2P ($M = Zr$ and Hf).

$$R_T = \frac{2\pi^2 k_B T m^* / \hbar e H}{\sinh(2\pi^2 k_B T m^* / \hbar e H)} \quad (1)$$

where m^* is the effective cyclotron mass. The fits yield small effective masses as collected in Table I. Particularly noteworthy is the very small $m^* = 0.046m_0$ for the α branch of Zr_2Te_2P at $F_\alpha = 11.4$ T, where m_0 is the free electron mass.

The calculated Fermi surfaces and band structures of Zr_2Te_2P and Hf_2Te_2P are shown in Fig. 5 and Fig. 7, respectively, revealing that they are quite similar. Fig. 6 compares the effect of the spin-orbit interaction on the pockets near the Γ point obtained in GGA with and without spin-orbit coupling for the Zr (top row) and Hf (bottom row) based 221 compound. Notice that in going from GGA-spin (left column) to GGA-spin+SOC (right column) the size of the orbits are not significantly affected for the Zr based compound. In the case of the Hf based compound, in the absence of SOC the smaller orbit is estimated to be significantly (about a factor of 2) larger than the smallest observed value of the oscillation frequency (~ 100 T). However, as can be seen from the bottom row of Fig. 6 the effect of SOC is to reduce the lowest orbit by a significant factor which brings the value of the smallest frequency (~ 80 T) in the observed range. Rough estimates of the size of the three lowest frequencies for the Zr based compound are ~ 30 T, $60 - 70$ T, $110 - 120$ T. For the case of the Hf based compound the three lowest frequencies are roughly $70 - 80$ T, $110 -$

120 T, and ~ 200 T. Fig. 7 presents the band structure for the Zr and Hf based compounds obtained with the inclusion of the SOC. They are very similar, where there are small differences in the size of the energy separation between the bands near Fermi level at the Γ point. This is also true at the K point for those bands closest to the Fermi level.

IV. CONCLUSION

We have used iodine vapor phase transport to grow single crystals of the compounds Zr_2Te_2P and Hf_2Te_2P . Measurements of the bulk electrical transport and thermodynamic properties indicate Fermi liquid behavior at low T . Both compounds readily exhibit quantum oscillations in magnetization measurements, from which we have determined the frequencies associated with several parts of the Fermi surfaces. Lifshitz-Kosevich fits to the temperature dependent amplitudes of the oscillations reveals small effective masses, with a particularly small value for the α branch of Zr_2Te_2P . Electronic structure calculations are presented that are in good agreement with these results. Calculations also indicate that measurements in higher magnetic fields will uncover larger Fermi surface sections with higher oscillation frequencies. Fits to the quantum oscillation data also provide preliminary evidence that some bands have a Berry's phase. This will be presented in detail in a separate manuscript.

These results make both Zr_2Te_2P and Hf_2Te_2P in-

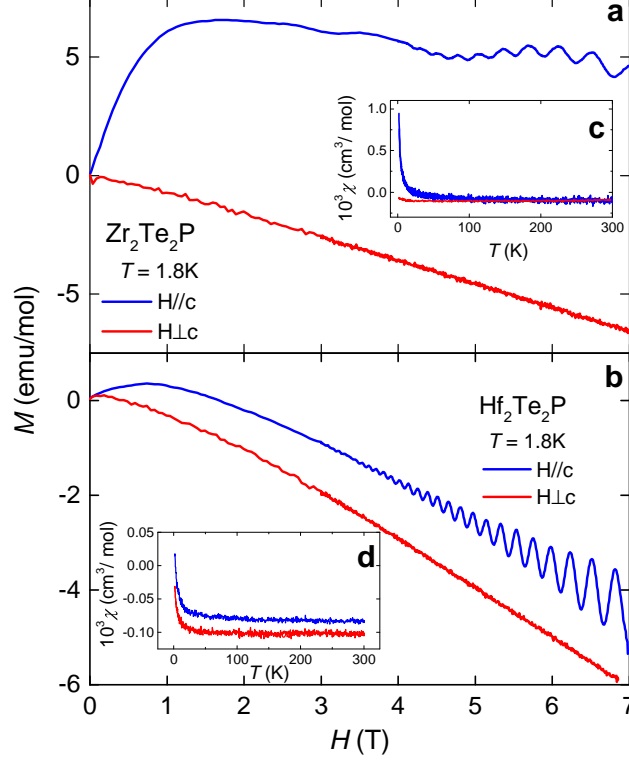


FIG. 3. (a) Magnetization M vs. magnetic field H for temperature $T = 1.8$ K for magnetic field H applied parallel \parallel and perpendicular \perp to the c -axis for $\text{Zr}_2\text{Te}_2\text{P}$. (b) Magnetic susceptibility $\chi = M/H$ vs. T for $H = 10$ kOe applied \parallel and \perp to the c -axis for $\text{Zr}_2\text{Te}_2\text{P}$. (c) M vs. H for 1.8 K for $H \parallel$ and \perp to the c -axis for $\text{Hf}_2\text{Te}_2\text{P}$ (d) χ vs. T for $H = 10$ kOe applied \parallel and \perp to the c -axis for $\text{Hf}_2\text{Te}_2\text{P}$.

TABLE I. Summary of results from fast Fourier transform (FFT) of quantum oscillations for $\text{Zr}_2\text{Te}_2\text{P}$ and $\text{Hf}_2\text{Te}_2\text{P}$. Frequencies $F(T)$ and effective masses $m^*(m_0)$ are listed.

	$F_\alpha(T), m_\alpha^*(m_0)$	F_β, m_β^*	F_γ, m_γ^*	F_η, m_η^*
Zr	11.4, 0.046	89.9, 0.22	—	—
Hf	—	—	106.8, 0.27	146.6, 0.22

triguing candidates for further study as potential hosts for Dirac physics. Of particular interest is to determine whether the calculated Dirac points that are away from the Fermi energy have an impact on the physical properties, or if the Fermi energy can be tuned to be closer to them. These materials are also particularly well suited to spectroscopic investigations such as ARPES, given the ease with which they are cleaved. This property also opens the possibility of device development. Finally, we point out that this family of materials likely can be expanded to include a variety of chemical analogues: e.g., $M_2\text{Te}_2\text{As}$ ($M = \text{Ti}, \text{Zr}, \text{and Hf}$) are likely to form.

V. ACKNOWLEDGEMENTS

This work was performed at the National High Magnetic Field Laboratory (NHMFL), which is supported by

National Science Foundation Cooperative Agreement No. DMR-1157490, the State of Florida and the DOE. A portion of this work was supported by the NHMFL User Collaboration Grant Program (UCGP). LB, DR, and SM are supported by DOE-BES through award de-sc0002613. TB and TS are supported by DOE-BES through award de-sc0008832.

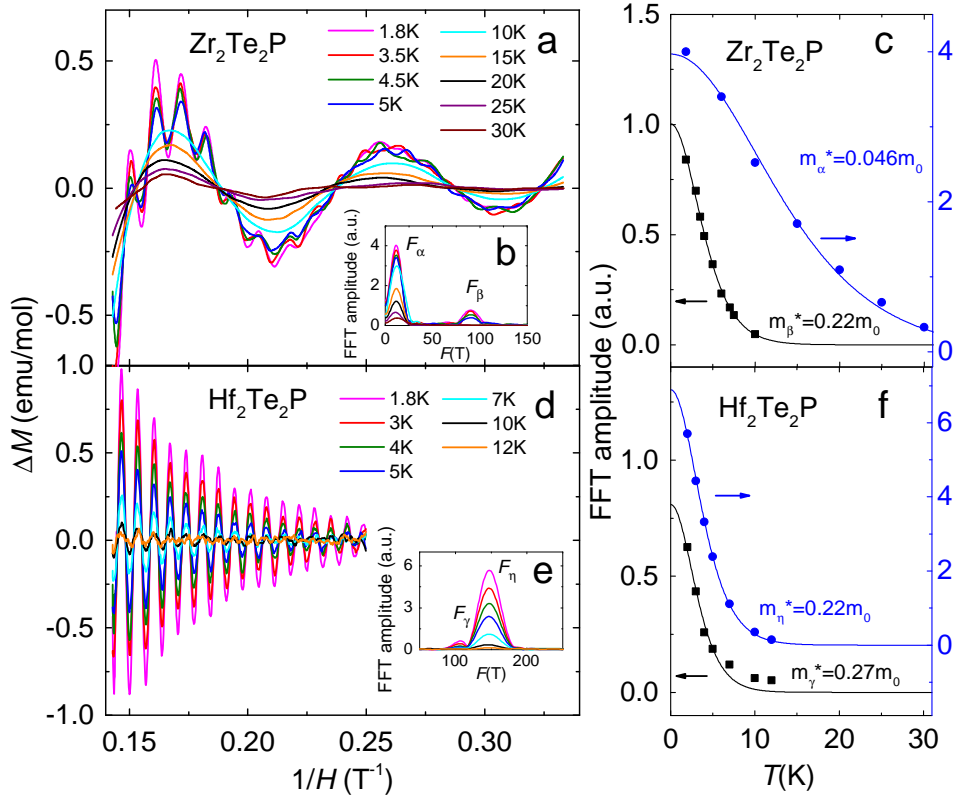


FIG. 4. (a) Background subtracted magnetization ΔM for $\text{Zr}_2\text{Te}_2\text{P}$ showing de Hass-van Alphen (dHvA) oscillations for different temperatures T between 1.8 K and 30 K in a field range $H = 3 \text{ T} - 7 \text{ T}$. ΔM is obtained by subtracting a 3rd order polynomial background from the raw data. (b) Fast Fourier transforms (FFT) for ΔM at various T s for $\text{Zr}_2\text{Te}_2\text{P}$. (c) Amplitude of the peaks observed in FFT spectra as a function of the temperature for $\text{Zr}_2\text{Te}_2\text{P}$. The solid lines are fits to the data using the Lifshitz-Kosevich formula. (d) ΔM for $\text{Hf}_2\text{Te}_2\text{P}$. (e) FFTs of ΔM at various T s (using a Hanning window) for $\text{Hf}_2\text{Te}_2\text{P}$. (f) T dependence of the FFT amplitude for ΔM for $\text{Hf}_2\text{Te}_2\text{P}$.

- ¹ H. Ji, I. Pletikosi, Q. D. Gibson, G. Sahasrabudhe, T. Valla, and C. R. J., arXiv:1512.00528 (2015).
- ² K. von Klitzing, Rev. Mod. Phys. **58**, 519 (1986).
- ³ H. L. Stormer, Rev. Mod. Phys. **71**, 875 (1999).
- ⁴ T. Wehling, A. Black-Schaffer, and A. Balatsky, Advances in Physics **63**, 1 (2014).
- ⁵ H. Zhang, C.-X. Liu, X.-L. Qi, X. Dai, Z. Fang, and S.-C. Zhang, Nat Phys **5**, 438 (2009).
- ⁶ Y. L. Chen, J. G. Analytis, J.-H. Chu, Z. K. Liu, S.-K. Mo, X. L. Qi, H. J. Zhang, D. H. Lu, X. Dai, Z. Fang, S. C. Zhang, I. R. Fisher, Z. Hussain, and Z.-X. Shen, Science **325**, 178 (2009).
- ⁷ D. Hsieh, Y. Xia, D. Qian, L. Wray, J. H. Dil, F. Meier, J. Osterwalder, L. Patthey, J. G. Checkelsky, N. P. Ong, A. V. Fedorov, H. Lin, A. Bansil, D. Grauer, Y. S. Hor, R. J. Cava, and M. Z. Hasan, Nature **460**, 1101 (2009).
- ⁸ Y. Xia, D. Qian, D. Hsieh, L. Wray, A. Pal, H. Lin, A. Bansil, D. Grauer, Y. S. Hor, R. J. Cava, and M. Z. Hasan, Nat Phys **5**, 398 (2009).
- ⁹ Z. K. Liu, J. Jiang, B. Zhou, Z. J. Wang, Y. Zhang, H. M. Weng, D. Prabhakaran, S.-K. Mo, H. Peng, P. Dudin,

- T. Kim, M. Hoesch, Z. Fang, X. Dai, Z. X. Shen, D. L. Feng, Z. Hussain, and Y. L. Chen, Nat Mater **13**, 677 (2014).
- ¹⁰ Z. Wang, H. Weng, Q. Wu, X. Dai, and Z. Fang, Phys. Rev. B **88**, 125427 (2013).
- ¹¹ Z. Wang, Y. Sun, X.-Q. Chen, C. Franchini, G. Xu, H. Weng, X. Dai, and Z. Fang, Phys. Rev. B **85**, 195320 (2012).
- ¹² Z. K. Liu, B. Zhou, Y. Zhang, Z. J. Wang, H. M. Weng, D. Prabhakaran, S.-K. Mo, Z. X. Shen, Z. Fang, X. Dai, Z. Hussain, and Y. L. Chen, Science **343**, 864 (2014).
- ¹³ H. Weng, C. Fang, Z. Fang, B. A. Bernevig, and X. Dai, Phys. Rev. X **5**, 011029 (2015).
- ¹⁴ B. Q. Lv, H. M. Weng, B. B. Fu, X. P. Wang, H. Miao, J. Ma, P. Richard, X. C. Huang, L. X. Zhao, G. F. Chen, Z. Fang, X. Dai, T. Qian, and H. Ding, Phys. Rev. X **5**, 031013 (2015).
- ¹⁵ S.-Y. Xu, I. Belopolski, D. S. Sanchez, C. Zhang, G. Chang, C. Guo, G. Bian, Z. Yuan, H. Lu, T.-R. Chang, P. P. Shibayev, M. L. Prokopovych, N. Alidoust, H. Zheng, C.-C. Lee, S.-M. Huang, R. Sankar, F. Chou, C.-H. Hsu, H.-T.

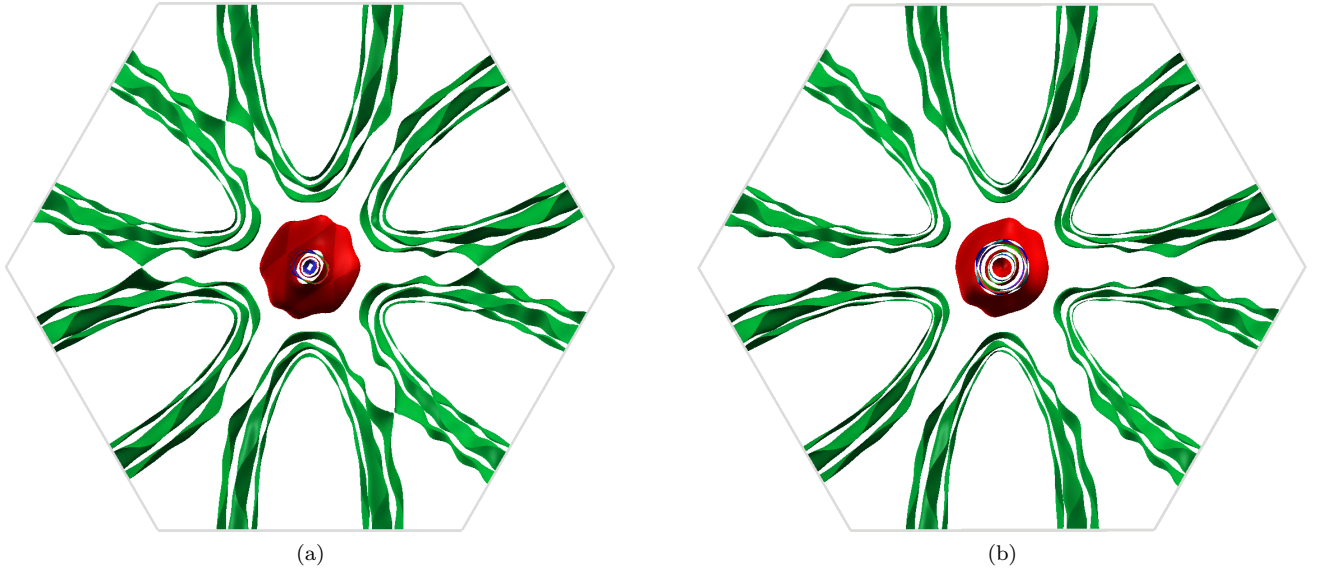


FIG. 5. (color-online) Comparison between the Fermi surface of the Zr (a) Hf (b) based 221 compounds.

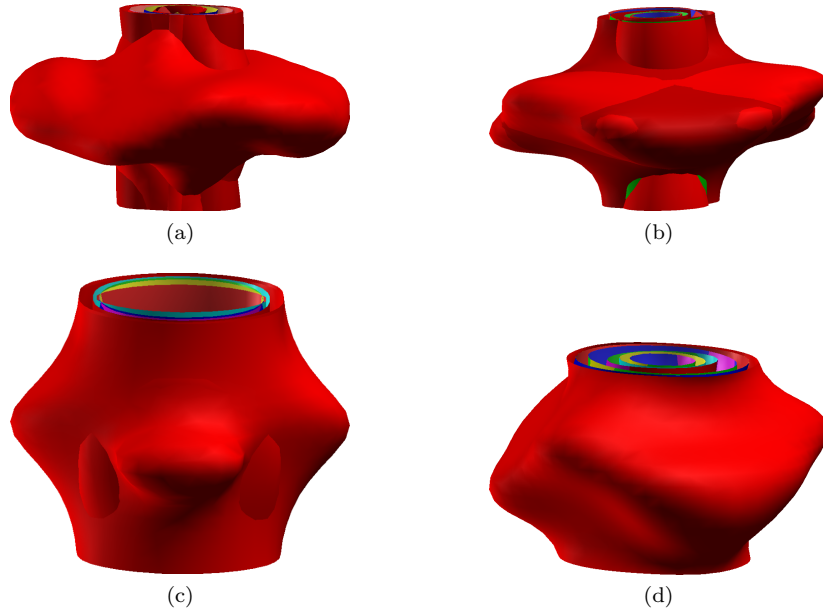


FIG. 6. (color-online) Comparison between the Fermi pockets near the Γ point obtained in GGA with (right column) and without (left column) spin-orbit coupling for the Zr (top row) and Hf (bottom row) based 221 compound.

- Jeng, A. Bansil, T. Neupert, V. N. Strocov, H. Lin, S. Jia, and M. Z. Hasan, *Science Advances* **1**, 1501092 (2015).
- ¹⁶ C. Shekhar, A. K. Nayak, Y. Sun, M. Schmidt, M. Nicklas, I. Leermakers, U. Zeitler, Y. Skourski, J. Wosnitza, Z. Liu, Y. Chen, W. Schnelle, H. Borrmann, Y. Grin, C. Felser, and B. Yan, *Nat Phys* **11**, 645 (2015).
- ¹⁷ M. Dzero, K. Sun, V. Galitski, and P. Coleman, *Phys. Rev. Lett.* **104**, 106408 (2010).
- ¹⁸ N. Xu, X. Shi, P. K. Biswas, C. E. Matt, R. S. Dhaka, Y. Huang, N. C. Plumb, M. Radović, J. H. Dil, E. Pom-jakushina, K. Conder, A. Amato, Z. Salman, D. M. Paul, J. Mesot, H. Ding, and M. Shi, *Phys. Rev. B* **88**, 121102 (2013).
- ¹⁹ J. Jiang, S. Li, T. Zhang, Z. Sun, F. Chen, Z. Ye, M. Xu, Q. Ge, S. Tan, X. Niu, M. Xia, B. Xie, Y. Li, X. Chen, H. Wen, and D. Feng, *Nat Commun* **4**, 3010 (2013).
- ²⁰ T. Liang, Q. Gibson, M. N. Ali, M. Liu, R. J. Cava, and N. P. Ong, *Nature Materials* **14**, 280 (2015).
- ²¹ L. P. He, Y. T. Jia, S. J. Zhang, X. C. Hong, C. Q. Jin, and S. Y. Li, *arXiv:1502.02509* (2015).

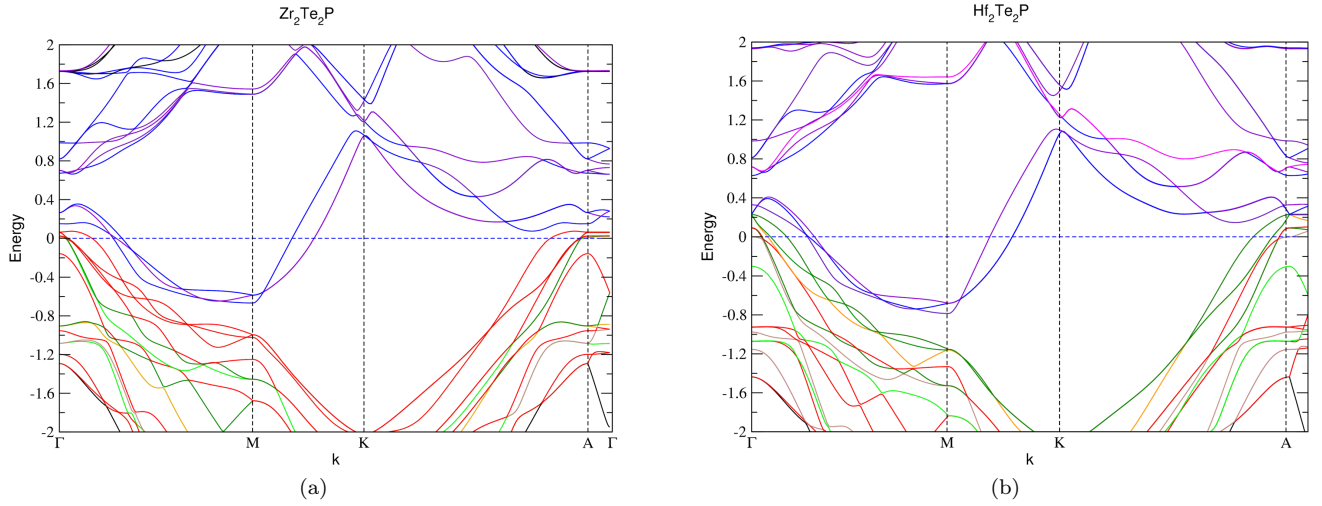


FIG. 7. (color-online) The electronic band structure of (a) the Zr-based and (b) Hf-based compound obtained with the inclusion spin-orbit interaction.

- ²² L. Aggarwal, A. Gaurav, G. S. Thakur, Z. Haque, A. K. Ganguli, and G. Sheet, *Nat Mater* **15**, 32 (2016).
- ²³ K. Tschulik, M. Ruck, M. Binnewies, E. Milke, S. Hoffmann, W. Schnelle, B. P. T. Fokwa, M. Gillisen, and S. P., *Eur. J. Inorg. Chem* **2009**, 3102 (2009).
- ²⁴ K. Stahl, “Winprep,” Lyngby, Denmark.
- ²⁵ M. Shishkin, M. Marsman, and G. Kresse, *Phys. Rev. Lett.* **99**, 246403 (2007).
- ²⁶ F. Fuchs, J. Furthmüller, F. Bechstedt, M. Shishkin, and G. Kresse, *Phys. Rev. B* **76**, 115109 (2007).
- ²⁷ M. Shishkin and G. Kresse, *Phys. Rev. B* **75**, 235102 (2007).
- ²⁸ M. Shishkin and G. Kresse, *Phys. Rev. B* **74**, 035101 (2006).
- ²⁹ J. P. Perdew, K. Burke, and M. Ernzerhof, *Phys. Rev. Lett.* **77**, 3865 (1996).
- ³⁰ P. E. Blöchl, *Phys. Rev. B* **50**, 17953 (1994).
- ³¹ A. Kokalj, *Comp. Mater. Sci.* **28**, 155 (2003), code available from <http://www.xcrysden.org>.
- ³² E. Teatum, J. Waber, and K. A. Gschneidner, “Compilation of calculated data useful in predicting metallurgical behavior of the elements in binary alloy systems,” Los Alamos Scientific Laboratory of the University of California (1960).